Tidal effects and the environment dependence of halo assembly

Oliver Hahn,[1*] Cristiano Porciani,[1,2] Avishai Dekel[3] and C. Marcella Carollo[1]

[1]*Department of Physics, ETH Zurich, 8093 Zurich, Switzerland*
[2]*Argelander Institut für Astronomie, Auf dem Hügel 71, 53121 Bonn, Germany*
[3]*Racah Institute of Physics, The Hebrew University, Jerusalem 91904, Israel*

ABSTRACT

We explore a possible origin for the puzzling anti-correlation between the formation epoch of galactic dark-matter haloes and their environment density. This correlation has been revealed from cosmological N-body simulations and is in conflict with the extended Press–Schechter model of halo clustering. Using similar simulations, we first quantify the straightforward association of an early formation epoch with a reduced mass-growth rate at late times. We then find that a primary driver of suppressed growth, by accretion and mergers, is tidal effects dominated by a neighbouring massive halo. The tidal effects range from a slowdown of the assembly of haloes due to the shear along the large-scale filaments that feed the massive halo to actual mass loss in haloes that pass through the massive halo. Using the restricted three-body problem, we show that haloes are prone to tidal mass loss within 1.5 virial radii of a larger halo. Our results suggest that the dependence of the formation epoch on environment density is a secondary effect induced by the enhanced density of haloes in filaments near massive haloes where the tides are strong. Our measures of assembly rate are particularly correlated with the tidal field at high redshifts $z \sim 1$.

Key words: methods: N-body simulations – galaxies: formation – galaxies: haloes – cosmology: theory – dark matter – large-scale structure of Universe.

1 INTRODUCTION

Dark-matter haloes provide the gravitational potential wells in which galaxies form, and as such, the understanding of their assembly process during the cosmological history is a key element in the theory of galaxy formation. Focusing on gravitational physics while avoiding the complications associated with baryonic physics, the study of the growth of dark-matter haloes is the straightforward, more solid part of the theory of galaxy formation. The process of bottom-up assembly of dark haloes is described successfully by an approximate formalism, the extended Press–Schechter (EPS) or excursion-set model, which combines the statistics of an initial Gaussian random fluctuation field with the gravitational instability theory of linear fluctuation growth and with the non-linear spherical collapse model (Press & Schechter 1974; Bond et al. 1991; Lacey & Cole 1993). In the simplest version of this model, the assembly history of a halo is predicted to be fully determined by its mass, independently of its environment (e.g. Bardeen et al. 1986; Efstathiou et al. 1988; Mo & White 1996). More sophisticated versions of the EPS do involve a certain environment dependence, but they do not recover the correlation seen in the simulations (Catelan et al. 1998; Taruya & Suto 2000). The mere mass dependence, motivated by

the simplest EPS model, lies at the basis of the widely used scheme for galaxy clustering that utilizes the halo occupation distribution (HOD) (see Cooray & Sheth 2002, and references therein).

However, numerical simulations of cosmological structure formation revealed that the halo assembly history does depend on the density of haloes in its environment (Sheth & Tormen 2004; Gao, Springel & White 2005; Wechsler et al. 2006; Harker et al. 2006; Maulbetsch et al. 2007; Hahn et al. 2007b; Gao & White 2007; Croton, Gao & White 2007; Jing, Suto & Mo 2007; Wetzel et al. 2007; Neistein & Dekel 2008; Angulo, Baugh & Lacey 2008; Li, Mo & Gao 2008; Fakhuri & Ma 2009a,b). For example, when the halo history is parametrized by a formation redshift $z_{\rm form}$ corresponding to the time by which the halo had assembled one half of its current mass, haloes that formed earlier are found to be more strongly clustered and, equivalently, reside in denser environments. This effect is valid for haloes that are much smaller than the current characteristic gravitationally collapsing mass-scale $M_*(\sim 10^{13}\,{\rm M}_\odot$ at redshift 0) and reverses for haloes above M_*. The origin of this and related deviations from the predictions of the EPS, sometimes termed 'assembly bias' (Gao & White 2007), is not obvious – it poses a very interesting open theoretical question which deserves a simple understanding.

There have been several attempts to understand the assembly bias. Sandvik et al. (2007) noted that the assembly bias can be incorporated in an excursion-set scenario where the spherical collapse

*E-mail: hahn@phys.ethz.ch

model is replaced by ellipsoidal collapse, and the density threshold for halo collapse depends on the shape and size of the local environment. Despite recovering some environment dependence, the effect found by these authors is too weak to explain the *N*-body results. However, Sandvik et al. (2007) considered only the tidal field generated by the linear (Gaussian) density perturbations, as derived by Doroshkevich (1970). *N*-body simulations indicate that at late times and small scales, the distributions of tidal field eigenvalues depart significantly from those for a Gaussian random field (see e.g. Hahn et al. 2007b). Environmental effects in the ellipsoidal collapse model have also been discussed by Desjacques (2008), but the model investigated by this author could not reproduce the correct sign of the assembly bias at low masses.

Wang, Mo & Jing (2007) found that small old haloes tend to reside next to very massive haloes. Considering the relative velocity of the dark-matter flow surrounding the haloes, they observed that particles surrounding the haloes with highest z_{form} have large relative velocities.

Most recently, Dalal et al. (2008) showed that the assembly bias at high masses follows naturally from the statistics of peaks of Gaussian random fluctuations when accounting also for the peak curvature. At low masses, these authors find a systematic trend of halo age with the velocity dispersion of the environment. Both Wang et al. (2007) and Dalal et al. (2008) suggest that the accretion on to a halo is suppressed because environmental velocities exceed the halo's virial velocity. A possible scenario leading to these high velocities is that the dark-matter fluid is 'hotter' in regions of higher density (see also Mo et al. 2005) after shell crossing during the formation of the host large-scale structure. This is difficult to reconcile with other findings that the dark-matter flow in dense filaments is rather 'cold' (e.g. Klypin et al. 2003). In particular, Sandvik et al. (2007) argue that the mass of the large-scale environment in which the low-mass haloes form is not large enough to account for this explanation. Furthermore, the measures employed by Wang et al. (2007) and Dalal et al. (2008) are not sensitive to distinguish between various scenarios: 'hot' flows, haloes that move against the flow of their environment on 'unorthodox' orbits (Ludlow et al. 2008) and strongly sheared flows.

In this article, we address the hypothesis that the early formation times of haloes of a given mass much below the non-linear mass in dense environments are primarily driven by the *tidal* suppression of the halo growth rate in the vicinity of a neighbouring massive halo. Small, typical (low-sigma) haloes tend to form in filaments (e.g. Porciani, Dekel & Hoffman 2002a), and stream along them into more massive, rare (high-sigma) haloes. The tidal field in these regions is likely to generate an ordered shear flow and thus suppress the halo growth by accretion or mergers. This suppression is expected to be correlated with the proximity to the massive halo. Those small haloes that have already passed through the inner regions of bigger haloes are likely to have lost mass due to tidal stripping (Gill, Knebe & Gibson 2005; Diemand, Kuhlen & Madau 2007; Ludlow et al. 2008) and thus show the earliest formation times.

In order to test this hypothesis, we quantify in several different ways the halo assembly history and its environment, and study the correlations between the adopted quantities. The traditional parametrization of assembly history via the formation epoch z_{form} is complemented with more direct measures of halo growth rate at different redshifts. The environment, commonly referred to by the halo number density or the amplitude of the two-point correlation function, is characterized instead by the tidal/shear field, via the eigenvalues of the deformation tensor. The correlations between

assembly history and environment are shown graphically and measured via correlation coefficients. The primary role of the tidal field over the density field is to be addressed by the relative strength of the corresponding correlations with the assembly history.

The outline of this article is as follows. In Section 2, we summarize the specifics of our *N*-body simulations and the dark-matter halo catalogues. In Section 3, we recover the dependence of halo formation times on environment density and clustering amplitude. In Section 4, we introduce further measures of halo assembly complementing a formation redshift. In Section 5, we define the relevant characteristics of the sheared flow around haloes and its tidal origin before we illustrate its relation to mass assembly. In Section 6, we demonstrate the role of tidal effects in the assembly bias by quantifying the correlation between the tidal field and the assembly rate, and comparing it to the correlation with environment density. We discuss our analysis in Section 7 and provide our conclusions in Section 8.

2 NUMERICAL SIMULATIONS

2.1 Specifics of the *N*-body simulations

We use a series of three high-resolution cosmological *N*-body simulations that were obtained with the tree-PM code GADGET-2 (Springel 2005). These simulations are used to follow the non-linear evolution of density perturbations in a flat Λ cold dark matter cosmology with a matter density parameter $\Omega_m = 0.25$, baryonic contribution $\Omega_b = 0.045$ and a present-day value of the Hubble constant $H_0 = 100 \, h \, \mathrm{km \, s^{-1}}$ with $h = 0.73$. The initial power spectrum has a long-wave spectral index of $n = 1$, and is normalized so that the rms fluctuation within a sphere of $8 \, h^{-1}$ Mpc linearly extrapolated to the present time is $\sigma_8 = 0.9$. Each of the three simulations follows 512^3 collisionless dark-matter particles in periodic boxes of sizes 45, 90 and $180 \, h^{-1}$ Mpc, respectively. Initial conditions were generated using the GRAFIC tool (Bertschinger 2001) at $z \simeq 79$, 65 and 52 for the three boxes. The corresponding particle masses are 4.7×10^7, 3.8×10^8 and $3.0 \times 10^9 \, h^{-1} \, \mathrm{M_\odot}$, respectively. Particle positions and velocities were saved for 30 time-steps, logarithmically spaced in expansion parameter a between $z = 10$ and 0. Unless otherwise stated, data from the simulation with the highest mass resolution, the $45 \, h^{-1}$ Mpc box, are used for the analysis of the lowest mass haloes. Results have been checked for resolution and box size effects against the other boxes.

2.2 Identification of haloes and the properties of their assembly

We identify bound structures using the standard friends-of-friends (FOF) algorithm (Davis et al. 1985) with a linking length equal to 0.2 times the mean inter-particle distance. Among all these dark-matter haloes, we keep only those haloes at $z = 0$ that fulfil the virialization constraint $|2T/V + 1| < 0.5$ (Bett et al. 2007), where T is the kinetic energy and V is the potential energy of the group of particles. In addition, we also exclude those groups where the most-bound particle is further than $R_{max}/4$ away from the centre of mass, where R_{max} is the distance of the furthest FOF particle from the group's centre of mass.

For each halo at redshift $z = 0$, we find its progenitors at any desired redshift $z > 0$ by identifying all the haloes that have particles in common with the final halo. At each snapshot, the most massive progenitor that contributes at least half of its particles to the final halo at $z = 0$ is identified as the 'main progenitor'. We define the formation redshift z_{form} of a halo of mass M_0 at $z = 0$ as the redshift
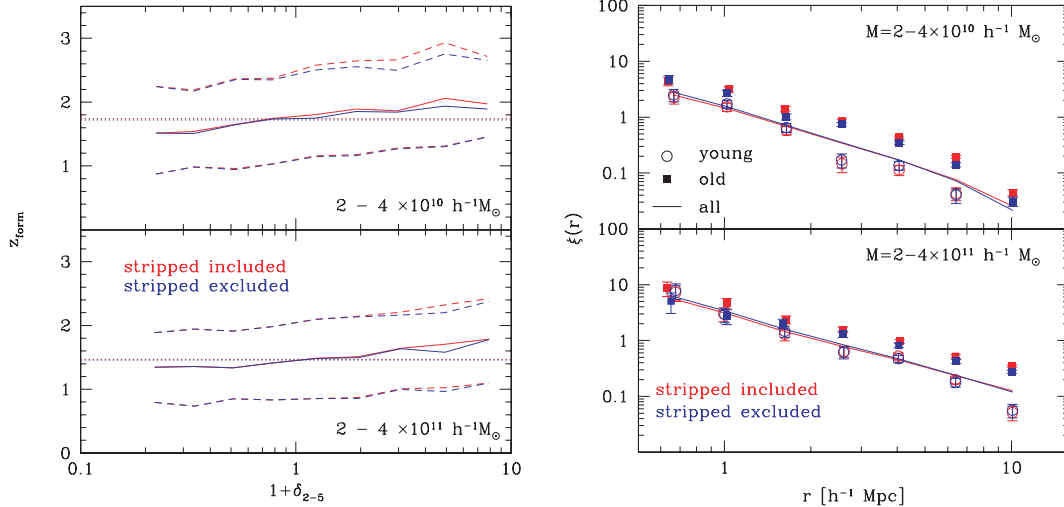
Figure 1. Left-hand panel: median formation redshift (solid line) as a function of the overdensity δ_{2-5} (see text for explanation) for all haloes, including those that experienced tidal mass loss (red) and only those haloes that never underwent such a mass loss (blue). The dashed lines indicate the 16th and 84th percentile in each bin. Results are shown for two different mass ranges, indicated in the respective panels. The dotted lines show the median formation redshift for each mass bin. Right-hand panel: two-point correlation functions for all haloes (solid lines) and for those haloes of given mass that have 20 per cent highest/lowest formation times (filled squares/open circles). Error bars correspond to Poisson errors. All results are shown including those haloes that experience tidal stripping of their mass (red) and excluding them (blue). See Section 2.2 for the definition of tidally stripped haloes.

at which a main progenitor with mass $M \geq M_0/2$ first appears in the simulation. The 'assembly history' of a halo, for our current purpose, is simply the mass-growth history of its main progenitor, $M(z)$.

In addition, we say that a halo underwent a 'mass-loss' event if between any successive snapshots along its history, it lost at least 3 per cent of its constituent particles to another more massive halo.[1]

3 THE DEPENDENCE OF FORMATION TIME ON ENVIRONMENT

The assembly bias has been detected using measures of either environment density or halo clustering. We first confirm these findings using our simulations.

3.1 Dependence on environmental density

At a fixed halo mass, the assembly bias can be measured as a systematic trend of halo formation time with the local density of the environment (e.g. Harker et al. 2006). We estimate the density at halo positions by smoothing the distribution of N-body particles on a given scale by convolving the particle positions with a spherical top-hat kernel of radius R. In practice, we first compute the density on a Cartesian grid using cloud-in-cell interpolation and then perform the convolution with the kernel using a fast Fourier transform (FFT). We denote with the symbol δ_R the mass overdensity computed using a smoothing radius of $R\,h^{-1}$ Mpc. Similarly, we call $\delta_{R_1-R_2}$ the overdensity computed within a spherical shell with an inner radius of $R_1\,h^{-1}$ Mpc and an outer radius of $R_2\,h^{-1}$ Mpc.

Fig. 1 (left-hand panel) shows the median and the 16th and 84th percentiles of z_f as a function of δ_{2-5} for our simulated haloes in two mass bins. We recover the trend found by Harker et al. (2006), and extend it to lower masses. We note that the removal of mass-losing

haloes from the sample makes a difference preferentially at high densities and at the high end of the z_f distribution. We will return to these haloes in Section 6.3 where we quantify their abundance.

3.2 Dependence on clustering amplitude

Alternatively, the assembly bias can be discussed in terms of the halo clustering amplitude. The two-point correlation function $\xi(r)$ is defined as the excess probability (with respect to random) to find two haloes in volume elements dV_1 and dV_2 separated by a comoving distance r,

$$dP_{12}(r) \equiv \bar{n}^2 \left[1 + \xi(r) \right] dV_1\, dV_2 , \tag{1}$$

where $\bar{n}$ indicates the mean halo number density. The assembly bias has been originally seen as a systematic dependence of the amplitude of $\xi(r)$ with halo formation time (Gao et al. 2005; Gao & White 2007). At constant halo mass, older haloes tend to be more strongly clustered than younger ones. The age dependence of the clustering amplitude is evident only for haloes with mass $M < M_*(z)$. Here $M_*(z)$ denotes the mass scale for which 1σ density fluctuations typically collapse at redshift z according to the Press–Schechter model. The linear rms overdensity on this mass scale has then to be $\sigma(M_*(z), z) = \delta_c \simeq 1.686$. At all redshifts, the number density of haloes with $M > M_*(z)$ is exponentially suppressed. In Fig. 1 (right-hand panel), we show how $\xi(r)$ changes with halo age in our simulations. The ratio of the different correlation functions agrees very well with the results of Gao & White (2007) and also extends the analysis to lower masses.

4 HALO MASS ASSEMBLY HISTORIES

In this section, we introduce measures of halo assembly complementing the common parametrization of assembly histories through the formation time.

---

[1] This is equivalent to a $\sim$5 per cent change in the measured formation redshift (see equation 4).

Table 1. Spearman rank correlation coefficients ρ_s between three different measures of a halo mass assembly: the formation redshift z_{form}, the assembly rate $A(z)$ and the mass-growth ratio $G(z)$. The coefficients are given for the progenitors of haloes identified at $z = 0$ with masses between 2 and $4 \times 10^{10}\,h^{-1}\,\text{M}_\odot$ (top) in the $45\,h^{-1}$ Mpc box and for haloes with masses between 2 and $4 \times 10^{11}\,h^{-1}\,\text{M}_\odot$ (bottom) in the $90\,h^{-1}$ Mpc box.

ρ_s	$z = 0$	$z = 0.5$	$z = 1$	$z = 2$
	$M(0) = 2 - 4 \times 10^{10}\,h^{-1}\,\text{M}_\odot$			
$(z_{\text{form}}, A(z))$	-0.58	-0.62	-0.65	-0.08
$(z_{\text{form}}, G(z))$	$-$	-0.40	-0.67	-0.87
$(A(z), G(z))$	$-$	0.42	0.32	0.16
	$M(0) = 2 - 4 \times 10^{11}\,h^{-1}\,\text{M}_\odot$			
$(z_{\text{form}}, A(z))$	-0.46	-0.57	-0.29	0.50
$(z_{\text{form}}, G(z))$	$-$	-0.40	-0.77	-0.81
$(A(z), G(z))$	$-$	0.36	-0.03	-0.30

4.1 The mass assembly rate of haloes

We define the current assembly rate of each halo by taking the time derivative of its smoothed assembly history $\mathcal{S}[M(z)]$, where $\mathcal{S}$ is some smoothing operation. From the smoothed assembly histories, we define the current assembly rate as (cf. Neistein, van den Bosch & Dekel 2006)

$$A(z) \equiv -\frac{\mathrm{d}}{\mathrm{d}z} \ln \mathcal{S}[M(z)]. \tag{2}$$

We apply smoothing by local regression (LOESS; Cleveland 1979), i.e. the data are fitted by a linear model inside a window, and the fit value is evaluated at the centre of each window position. A window of 0.5 in redshift proved to be well suited and has been used in our analysis. It is necessary to smooth since the assembly histories of single haloes are prone to fluctuations that are due to the intrinsic stochasticity of the simulation/halo-identification process.

In close analogy to the definition of the formation redshift, we will use the ratio $G(z) \equiv M(0)/M(z)$ between the final mass and the mass at redshift z as the 'forward' measure of halo growth since redshift z.

Both quantities $A(z)$ and $G(z)$ are strongly related with the integral measure z_{form} [note that $G(z_{\text{form}}) = 2$ by definition of z_{form}]. In Table 1, we show the Spearman rank correlations between these different measures as a function of redshift for the main progenitors of haloes with masses between 2 and 4×10^{10} and 2 and $4 \times 10^{11}\,h^{-1}\,\text{M}_\odot$ at $z = 0$. The median formation redshift for the first sample of haloes is 1.71, while it is 1.44 for the latter. We use the rank correlation coefficient rather than the linear Pearson correlation coefficient as it does not assume a linear relation between the correlated quantities.

For haloes of a given mass at $z = 0$, a large (small) $G(z)$ at high redshift implies trivially that the main progenitor mass was already high (low) at that epoch so that its formation time is high (low). The progenitor then also has a high (low) assembly rate $A(z)$ at early times and a low (high) $A(z)$ at late times.

Thus, a high formation redshift is related to a low assembly rate $A(z)$ at late times ($z \lesssim z_{\text{form}}$) and a high assembly rate at early times ($z \gtrsim z_{\text{form}}$). The latter can be seen for the higher mass sample where the median formation redshift is sufficiently low so that the correlation coefficient changes sign at $z = 2$. At late times, the formation redshift depends most sensitively on the assembly rate around $0.5 \lesssim z \lesssim 1$ for the low-mass sample and around $z \sim 0.5$ for the higher mass sample.

4.2 The influence of mass loss on formation time

While typical analytic models of structure formation predict a monotonous growth of halo mass over time, haloes do undergo interactions with other haloes which can lead to tidal mass loss. The influence of such a mass-loss event on the measured formation time of a halo can be estimated as follows. Several studies of structure formation in a bottom-up scenario (e.g. van den Bosch 2002; Wechsler et al. 2002) have suggested that the bulk of haloes assembles the mass exponentially with redshift:

$$M(z) = M(0)\exp(-\alpha z) \tag{3}$$

where α is the mass assembly rate. In this case, $z_{\text{form}} = \alpha^{-1}\log 2$. Let us assume that the smooth mass accretion history is interrupted at redshift z_{loss} by a single mass loss of $M_{\text{loss}} \equiv x\,M(z_{\text{loss}})$. For simplicity, the growth rate α is assumed to be identical before and after z_{loss} (it is trivial to extend our results to the most general case). A short calculation shows that a mass loss leads to an increase in measured formation redshift given by

$$z_{\text{form}} = \frac{1}{\alpha}\ln\frac{2}{1-x}. \tag{4}$$

5 THE EFFECT OF TIDAL FORCES ON THE ASSEMBLY OF HALO MASSES

In this section, we will demonstrate that the proximity to a massive halo provides a special environment for the formation and evolution of lower mass haloes due to tidally sheared flows influencing their assembly.

5.1 Halo evolution in the proximity to a massive halo

For a large number of haloes in our simulation, we investigated the evolution of their Lagrangian patches and of their Lagrangian environments. At all epochs, the Lagrangian patch of a halo is defined by the set of particles that are identified as part of the halo at $z = 0$. Similarly, we define the Lagrangian environment as the set of particles that in the initial conditions of the simulations were lying within a cube of $3\,h^{-1}$ Mpc centred on the corresponding Lagrangian patch. We observe significant differences between old and young haloes of a given mass.

The older haloes are preferentially found in a pronounced large-scale structure already at high redshifts, while this is not true for the younger haloes. In Fig. 2, we show the evolution of the particles making up two different haloes at $z = 0$ together with their Lagrangian environment. One of the haloes has a very high formation redshift of $z_{\text{form}} = 3.1$, while the other halo has a low formation redshift of $z_{\text{form}} = 0.42$. It is evident from the evolution of the environment of the old halo that, once the host filament formed, its neighbouring haloes show an expanding, 'Hubble-like', motion along the filament, which is not present for the younger halo. In the rest frame of the halo, this expansion along the filament appears as a recession of the neighbouring haloes in that direction. Remarkably, in both cases, the last major merger occurs perpendicular to the host large-scale structure. Thus, the gravitational shear accelerates the collapse perpendicular to the filament, while it slows down the collapse along the filament (cf. Porciani et al. 2002a; Porciani, Dekel & Hoffman 2002b). Tidal forces are expected to increase substantially in the vicinity of very massive haloes leading to a strong correlation between the tidal field and the density field on larger scales. This leads to the correlation of halo properties that are influenced by the external tidal field with the density field.
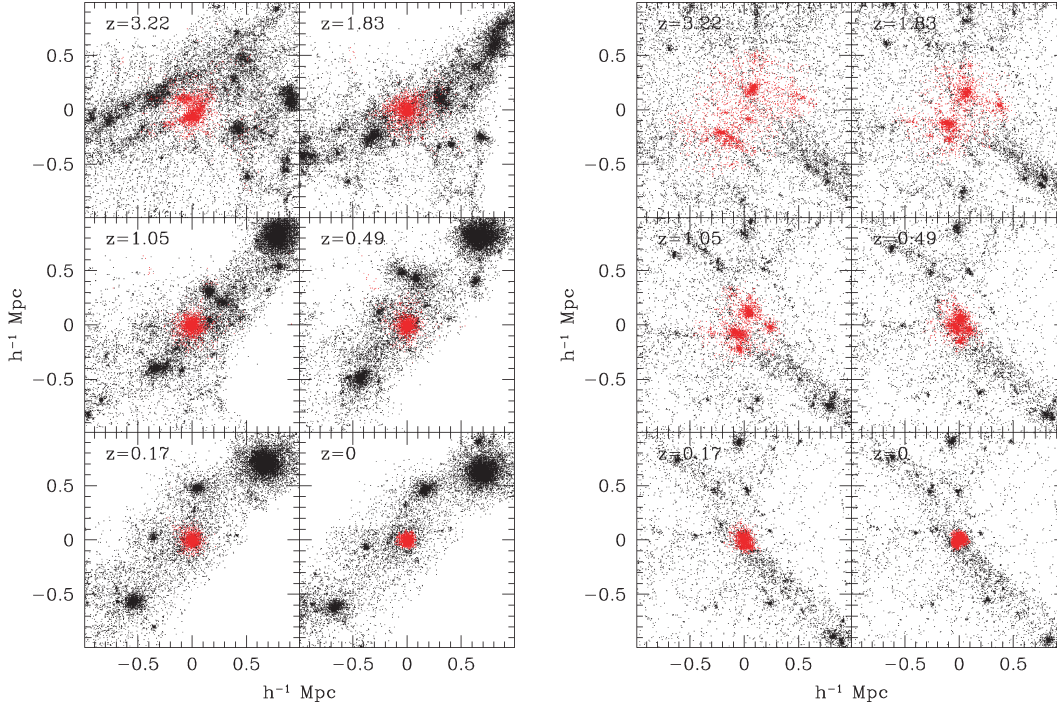
Figure 2. Evolution of the Lagrangian patch and environment of two haloes with mass $1.4 \times 10^{11} \, h^{-1} \, M_\odot$ at $z = 0$ and formation redshift $z_{\text{form}} = 3.1$ (left-hand panel) and $z_{\text{form}} = 0.42$ (right-hand panel). Particles that will constitute the halo at $z = 0$ (the Lagrangian patch) are shown in red, while particles that are contained in a $3 \, h^{-1}$ Mpc cube centred on the patch (the Lagrangian environment) are shown in black. The centre of the coordinate system moves with the centre of mass of the particles that constitute the halo at $z = 0$.

5.2 Quantifying sheared flows

The dynamics of dark-matter flows (and thus the accretion on to dark-matter haloes) are regulated by the gradient of the gravitational potential $\nabla\phi$, its Laplacian $\nabla^2\phi$ and the tidal tensor

$$T_{ij} = \left[\frac{\partial^2}{\partial_i \partial_j} - \frac{1}{3} \delta_{ij} \nabla^2 \right] \phi, \tag{5}$$

where δ_{ij} denotes the Kronecker symbol. The presence of a massive halo that locally dominates the gravitational potential generates a strong tidal field in its neighbourhood. Over time, the tidal field produces a tidally induced shear in the velocity field of the surrounding particles. The flow is stretched in the direction of the massive halo and compressed in the plane perpendicular to it. Since haloes preferentially reside in filaments or sheets (see e.g. Hahn et al. 2007b), tidal forces tend to accumulate coherently. This should impact the mass accretion history of smaller haloes neighbouring the massive one. To probe the influence of tidal forces, we quantify the velocity field surrounding small-mass haloes by expanding the local (peculiar) flow with respect to the bulk motion of the halo up to linear order in the distance x from the halo centre

$$v_i = \frac{\partial v_i}{\partial x_j} x_j. \tag{6}$$

We next perform a least-squares fit of the nine components of the velocity gradient tensor within one and four virial radii around each halo (cf. Porciani et al. 2002a,b). It is then possible to write the velocity gradient tensor as the sum of a symmetric and an anti-symmetric part

$$\frac{\partial v_i}{\partial x_j} = \frac{1}{2} \left(\frac{\partial v_i}{\partial x_j} + \frac{\partial v_j}{\partial x_i} \right) + \frac{1}{2} \left(\frac{\partial v_i}{\partial x_j} - \frac{\partial v_j}{\partial x_i} \right) \tag{7}$$

$$\equiv D_{ij} + \Omega_{ij}, \tag{8}$$

where D_{ij} corresponds to the rate-of-strain tensor and Ω_{ij} describes rigid rotation due to non-zero vorticity $\omega_i \equiv (\nabla \times \boldsymbol{v})_i = -\epsilon_{ijk}\Omega_{jk}$, where ϵ_{ijk} is the Levi-Cività symbol. The rate-of-strain tensor can be further decomposed as $D_{ij} \equiv \theta \, \delta_{ij} + \Sigma_{ij}$, where θ denotes the velocity divergence (or expansion scalar) and Σ_{ij} is the traceless shear tensor with eigenvalues $\mu_1 \leq \mu_2 \leq \mu_3$. For growing-mode fluctuations in the linear regime, $T_{ij} \propto \Sigma_{ij}$ and therefore the eigenvectors of these matrices are aligned. However, the proportionality of the shear and tide is broken by higher order terms. In general, the eigenvectors of the tensors remain parallel, but the eigenvalues evolve differently with time (e.g. Bertschinger & Jain 1994).[2] In fact, while tides act as sources for the velocity shear, the latter is also influenced by the velocity gradient, vorticity and the shear itself. In what follows, we use the velocity shear as a measure of the integrated effect of the gravitational tides after investigating the connection between the two in Section 5.3.

Both random motion and non-linear ordered motion will be superimposed on to the ordered linear deformation, as defined in equation (6), so that we can define a velocity dispersion along the three main axes of the rate-of-strain tensor quantifying this residual by

$$\sigma_i^2 \equiv \left\langle \left((\boldsymbol{v} - \lambda_i \boldsymbol{x} - \boldsymbol{\omega} \times \boldsymbol{x}) \cdot \boldsymbol{w}_i \right)^2 \right\rangle, \tag{9}$$

where $\lambda_1 \leq \lambda_2 \leq \lambda_3$ are the eigenvalues and $\boldsymbol{w}_i$ are the corresponding eigenvectors of the rate-of-strain tensor D_{ij}. Furthermore, we define a simple relative velocity $\boldsymbol{v}_{\text{rel}}$ between a halo's centre of mass velocity and the mean velocity of the region between one and four virial radii. If the velocity field is completely linear, then both $|\boldsymbol{v}_{\text{rel}}| = 0$ and $|\boldsymbol{\sigma}| = 0$. We observe that, apart from very little scatter,

---

[2] This holds in the Lagrangian frame before shell crossing (see also Barnes & Rowlingson 1989).

$|\boldsymbol{\sigma}|$ is completely dominated by $|\boldsymbol{v}_{\mathrm{rel}}|$. Non-zero $|\boldsymbol{\sigma}|$ and $|\boldsymbol{v}_{\mathrm{rel}}|$ can arise when the velocity grows non-linearly with distance from the halo, due to the presence of other haloes within 1–4 virial radii or in special circumstances when the halo has indeed a relative velocity with respect to its surrounding flow. We will return to this last aspect in Section 6.3. Furthermore, noise in the velocity field due to finite numerical resolution will also increase $|\boldsymbol{\sigma}|$ by causing spurious deviations from a flow with constant strain and thus impacting the goodness of the fit (see also Section 6.1).

5.3 The tidal origin of sheared flows

In this section, we will provide evidence that the tidal field due to a neighbouring massive halo induces shear in the dark-matter flow surrounding smaller haloes in its vicinity. To this end, we will compare the constant strain approximation (CSA in what follows) introduced in the previous section, i.e. that the flow is described by D_{ij} in equation (8), to a restricted three-body approximation for the tidal field. This will allow us to use the shear measured from the flow to quantify the importance of tides on the mass assembly of haloes in the rest of the paper.

Consider the restricted three-body problem, consisting of a larger body of mass M, a smaller body of mass $m \ll M$ and a third of negligible mass. The third body can have stable circular orbits around the smaller mass m only within the Hill radius

$$r_{\mathrm{Hill}} \simeq d \left(\frac{m}{3M} \right)^{1/3}, \tag{10}$$

where d is the distance between m and M (for a detailed derivation we refer the reader to Murray & Dermott 2000). Since in cosmological context, we do not have the idealized situation of the restricted three-body problem, we define the Hill radius of each halo as the minimal Hill radius due to any of its neighbours.[3] Now, given that the eigenvalues of the tidal tensor T_{ij} for a point mass M at a distance d are given by

$$\{\tau_i\} \equiv \left\{ -\frac{GM}{d^3}, \ -\frac{GM}{d^3}, \ \frac{2GM}{d^3} \right\}, \tag{11}$$

this choice is equivalent to selecting that neighbour which has maximal tidal influence GM/d^3 – the tidally dominant neighbour halo. The eigenvector $\boldsymbol{t}_3$ associated with the third eigenvalue τ_3 points radially towards the mass M, while $\boldsymbol{t}_1$ and $\boldsymbol{t}_2$ span the perpendicular plane but are otherwise undetermined due to the symmetry of the problem.

By investigating the flux through the Hill sphere (with volume V_{Hill} and surface $\partial V_{\mathrm{Hill}}$), it is then possible to connect the sheared motion of the flow around a halo, measured using the CSA defined

in Section 5.2, to the tidal forces due to the neighbouring halo. This flux is given by

$$\Phi \equiv \int_{\partial V_{\mathrm{Hill}}} \boldsymbol{v} \cdot \mathrm{d}\boldsymbol{A} \tag{12}$$

$$= \int_{V_{\mathrm{Hill}}} \nabla \cdot \boldsymbol{v} \, \mathrm{d}V \simeq \frac{4\pi}{3} r_{\mathrm{Hill}}^3 (\lambda_1 + \lambda_2 + \lambda_3), \tag{13}$$

where the first equality is just an application of the divergence theorem and the second follows after applying the CSA to the flow where the λ_i are assumed to be constant within r_{Hill}.

In order to verify that the shear measured in the flow indeed satisfies the CSA, we can rewrite equation (13) as

$$\frac{\langle v_{\mathrm{r}} \rangle}{r_{\mathrm{Hill}}} \simeq \frac{1}{3} (\lambda_1 + \lambda_2 + \lambda_3), \tag{14}$$

where $\langle v_{\mathrm{r}} \rangle$ is the mean radial velocity at r_{Hill}. Written this way, the left-hand side is independent of the assumption of constant strain. We can thus verify the validity of equation (14) directly in the N-body simulations in order to assert that the CSA is justified. In Fig. 3, we show $\langle v_{\mathrm{r}} \rangle / r_{\mathrm{Hill}}$ as a function of the mean of the strain eigenvalues for haloes with $r_{\mathrm{Hill}} < 4 r_{\mathrm{vir}}$, the range used when fitting the CSA flow model. The mean radial velocity was measured using the closest 100 particles outside the Hill sphere. Results are shown for haloes that have final masses at $z = 0$ between 2 and $4 \times 10^{10} \, h^{-1} \, \mathrm{M}_{\odot}$. The rank correlation is $\rho_{\mathrm{s}}(\langle v_{\mathrm{r}} \rangle / r_{\mathrm{Hill}}, \sum_i \lambda_i / 3) = 0.74$. This very strong correlation indicates that the constant strain model serves well to predict the flux into the Hill sphere.

In addition, we can directly check whether λ_3 is probing the tidal influence due to a neighbouring halo in which case we expect that $\lambda_3 \propto \tau_3$. Since $\tau_3 \propto M/d^3$ is a positive definite quantity, we show the shear eigenvalue μ_3, which has the same property, as a function of M/d^3 in the right-hand panel of Fig. 3. Results are given at three redshifts for the progenitors of haloes with masses between 2 and $4 \times 10^{10} \, h^{-1} \, \mathrm{M}_{\odot}$. We find a tight connection between the two quantities which is also reflected in the high rank correlations given in Table 2.

Finally, we can also verify whether the tidal field eigenvector $\boldsymbol{t}_3$, which is simply the normalized vector pointing radially towards the tidally dominant halo, is parallel to the third eigenvector $\boldsymbol{w}_3$ of the strain tensor and perpendicular to the first and the second, as would be expected if tides are inducing shear in the flow. Fig. 4 shows the distribution of the cosine of the angles between these vectors, i.e.

$$|\cos \theta_i| = \left| \frac{\boldsymbol{w}_i \cdot \boldsymbol{t}_3}{\|\boldsymbol{w}_i\|} \right| \tag{15}$$

at three redshifts in the simulation. If the strain on the fluid is indeed caused by the tidal field due to the neighbouring halo, then an alignment angle $|\cos \theta_3| \simeq 1$ is expected which is consistent with the results shown in Fig. 4. It is interesting to see that the degree of alignment – reflected in the width of the distributions – is slightly decreasing with decreasing redshift.

The findings presented in this section – in particular (1) that the rate-of-strain eigenvalue λ_3 is very strongly correlated with the tidal field eigenvalue due to the tidally dominant neighbour halo and (2) that the associated rate-of-strain eigenvector points into the direction of this halo – lead us to conclude that λ_3 can be used as a proxy to quantify the integrated effect of tides on the flow surrounding haloes in our subsequent analysis.

---

[3] This will possibly overestimate the Hill radius. The restricted three-body problem applies to the orbit of a test particle of zero mass around the mass m. While in the case of smooth accretion the third body can indeed be thought of as having negligible mass, in the case of mergers, the restricted three-body problem is of course of limited applicability.

Furthermore, the presence of finite masses other than m and M makes it unfortunately impossible to use radial acceleration vectors to find the region of gravitational influence of the second body m. Any self-bound mass (e.g. subhaloes or other tiny haloes outside the virial radius) will produce a dip in the potential. In order to use acceleration vectors it would be necessary to remove all structures smaller than the halo itself, which is practically impossible. In fact, for the same reasons we consider the shear tensor rather than the tidal tensor since the latter is affected by the same problems. Shear is the integrated result of tidal forces and thus probes directly their effect on the flow at the relevant scales.
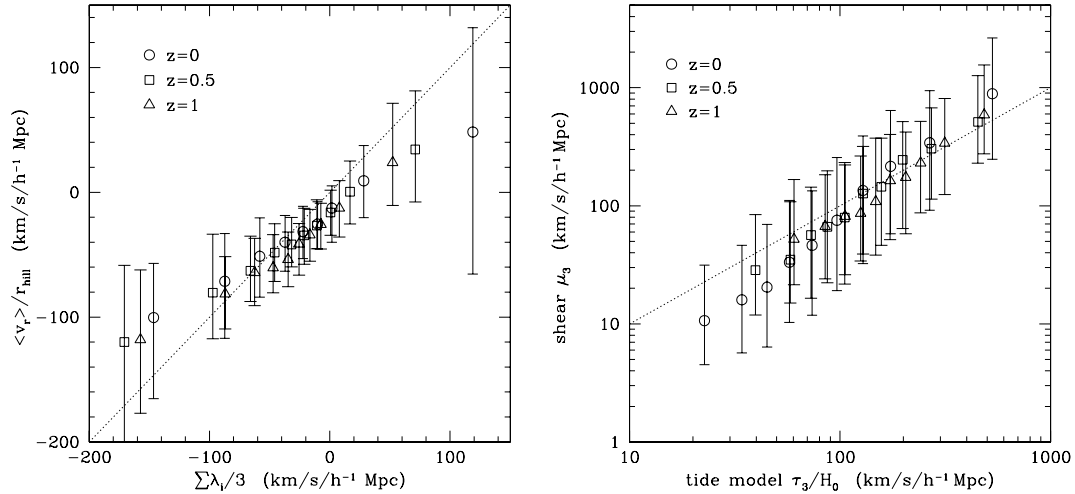
Figure 3. Comparisons between the flux on to haloes from particle velocities and in the CSA model, and between the tides due to the tidally dominant neighbour halo and measured shear in the CSA. Left-hand panel: the flow through the Hill sphere $\sum_i \lambda_i/3$ from the linear fit to the flow against median $\langle v_r \rangle / r_{\text{Hill}}$ measured directly from the simulation. Results are shown for haloes with $r_{\text{Hill}} \leq 4r_{\text{vir}}$, the region used for determining the λ_i. Right-hand panel: median eigenvalue of the shear tensor μ_3 measured from the flow as a function of the tidal force due to the tidally dominant neighbour halo $\tau_3 = 2GM/R^3$. Error bars show the 16th and 84th percentiles in each bin. Bins are chosen to include equal numbers of data points. The dotted lines indicate $x = y$. Data are given for the progenitors of haloes with masses between 2 and $4 \times 10^{10} \, h^{-1} \, \text{M}_\odot$.

Table 2. Spearman rank correlation coefficients ρ_s between the largest tidal field eigenvalue due to the tidally dominant neighbour and the strain eigenvalues λ_3 and shear eigenvalues μ_3, respectively. The coefficients are given for haloes identified at $z = 0$ with masses between 2 and $4 \times 10^{10} \, h^{-1} \, \text{M}_\odot$.

ρ_s	$z = 0$	$z = 0.5$	$z = 1$
$(\lambda_3, M/d^3)$	0.62	0.64	0.61
$(\mu_3, M/d^3)$	0.75	0.64	0.57

5.4 The tidal influence on mass assembly

The assembly of haloes is regulated by the amount of accretable material in their vicinity. The sphere of gravitational influence of a halo is bounded by the Hill sphere; only particles within it are potentially accretable. We will in this section quantify differences in the supply of accretable material and its relation to mass growth and tides.

In Fig. 5 (left-hand panel) we show the cumulative distribution of Hill radii (in units of virial radii) for the $z = 0.5$ progenitors of haloes with masses between 2 and $4 \times 10^{10} \, h^{-1} \, \text{M}_\odot$ and for these haloes at $z = 0$. The data are shown for all haloes and for those with the 20 per cent highest and lowest current assembly rates $A(z)$. We find that at both redshifts the estimated Hill radii of the least accreting haloes are significantly smaller than those of the most accreting haloes, which are comparable to those of all haloes. This implies that haloes with the lowest assembly rates experience stronger tidal fields than all other haloes.

The mass assembly rate $A(z)$, which can also be thought of as the mass flux through the halo surface

$$\frac{dM_h}{dt} = \int_{\partial V_{\text{vir}}} \rho \, \boldsymbol{v} \cdot d\boldsymbol{S}, \qquad (16)$$

is expected to be correlated through the continuity equation to the supply rate of accretable material. The latter is the mass flux through
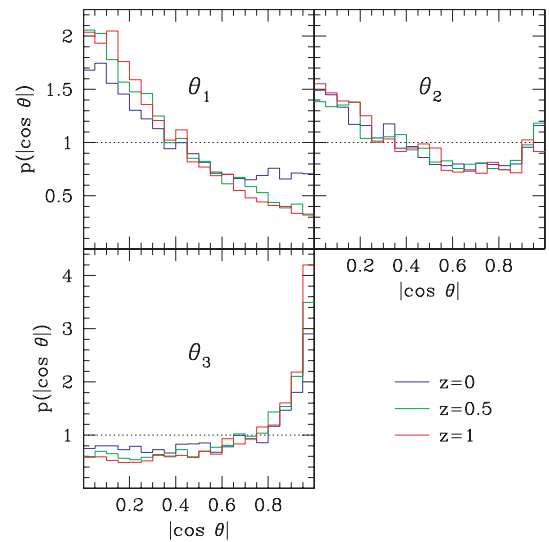

Figure 4. The probability distributions of angles $|\cos \theta_i|$ between the three rate-of-strain eigenvectors $\boldsymbol{w}_i$ and the direction to the tidally dominant neighbour halo for the progenitors of haloes with $z = 0$ masses between 2 and $4 \times 10^{10} \, h^{-1} \, \text{M}_\odot$ for three different redshifts: $z = 0$ (blue), $z = 0.5$ (green) and $z = 1$ (red). The black dotted line indicates a random distribution of angles.

the Hill sphere

$$\phi_{\text{Hill}} \equiv \int_{\partial V_{\text{Hill}}} \rho \, \boldsymbol{v} \cdot d\boldsymbol{S}. \qquad (17)$$

In both definitions ρ is the matter density and M_h is the halo mass. This correlation is, however, likely to be weakened by several factors. A particle does not enter the Hill sphere and the virial radius simultaneously, especially when the Hill radius is large, leading to a time-delayed correlation with the delay depending on the size of r_{Hill}. Furthermore, the Hill radius shrinks linearly with the distance to a more massive halo (see equation 10). In addition, the tidal field will also perturb particle trajectories inside the Hill sphere. Thus,
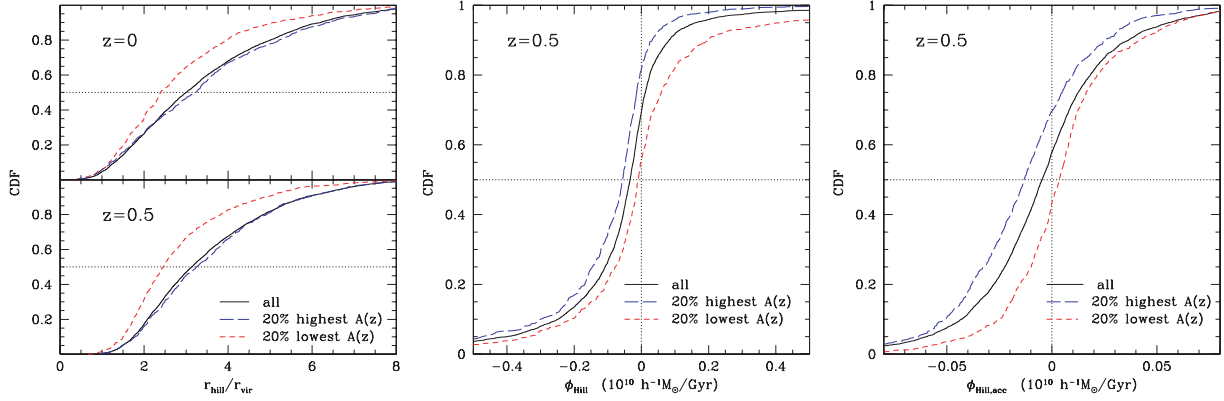
Figure 5. Left-hand panel: CDF of Hill radii in units of virial radii and (middle) CDFs of the mass flux through the Hill sphere; right-hand panel: same as the middle panel but only for low-velocity particles with $v < v_{vir}$. All data are shown for the progenitors at $z = 0.5$ of haloes with final masses between 2 and $4 \times 10^{10} \, h^{-1} \, M_\odot$ (and also at $z = 0$ for the left-hand panel). The CDFs are shown in black for the sample of all these haloes and in red (blue) for those haloes with the 20 per cent lowest (highest) assembly rate $A(z)$. Stripped haloes are excluded.

entering the Hill sphere is a necessary but not sufficient condition for a particle to be accreted in the future. Nevertheless, we can compare the flux through the Hill sphere for haloes with high and low assembly rates to probe the supply of accretable material and its relation to the assembly behaviour of haloes. In Fig. 5, middle panel, we show cumulative distributions of the flux through the Hill sphere for haloes with highest and lowest current assembly rates $A(z)$. The flux was computed using the closest 100 particles outside the Hill sphere from

$$\phi_{Hill} \simeq 4\pi \, R_{Hill}^2 \, \langle v_r \, \rho \rangle, \tag{18}$$

where v_r is the radial velocity and $\langle \cdot \rangle$ denotes the average over the shell occupied by the 100 particles. We find that the Hill sphere flux of the least accreting haloes is shifted towards more positive values relative to the most accreting sample, i.e. the flux into the Hill sphere is reduced for the least accreting haloes. In particular, these haloes have a median flux very close to zero.

Particles that enter the Hill sphere might not be accretable if they have too high velocities to be captured by the halo (see also Wang et al. 2007). In the plane perpendicular to the eigenvector belonging to τ_3 the tidal field compresses the flow and thus accelerates particles on to the halo. Furthermore, high velocities could also be due to particles orbiting the bigger halo which has a larger circular velocity than the smaller halo. To quantify the abundance of these particles that are potentially too fast for the halo to be captured, we determine the fraction of particles entering the Hill sphere that have a velocity smaller than the circular velocity. This is a conservative requirement since the halo should be able to capture particles up to its escape velocity (which is twice its circular velocity). We thus recompute the flux through the Hill sphere using only these accretable particles. In Fig. 5 (right-hand panel), the cumulative distributions of accretable fluxes are shown for the same halo samples as before. We find that the difference between the distributions increases slightly, the median flux through the Hill sphere is still very close to zero (if not slightly positive) for the least accreting haloes, while it is negative for the most accreting haloes.

These results suggest that accretion is not primarily limited by high velocities since the difference between the flux distributions does not change substantially when considering all particles as opposed to only slow particles. Hence, non-accreting haloes do not even draw on a supply of slow particles suggesting that they are

no longer convergence points in the local flow of dark-matter particles.[4]

5.5 The shear flow near early forming haloes

We will now discuss the connection between a sheared velocity field surrounding low-mass haloes and their mass assembly properties, thus providing further evidence for an influence of external tides on a mass assembly.

In Fig. 6, we show the cumulative distribution functions (CDFs) of the eigenvalues λ_i of the deformation tensor D_{ij} for haloes with highest and lowest assembly rates A at $z = 0.5$, where the effect is strongest. We observe a systematic shift of λ_2 and λ_3 towards more positive values for those haloes that grow slower. This implies that the flow around these haloes is more strongly sheared. As discussed in Section 5.3, sheared motion in the flow provides clear evidence

---

[4] Note that the relatively low flux through the Hill sphere for the most accreting haloes appears to be in conflict with their assembly rates and thus the growth they should experience. This incongruity is, however, easily resolved by considering the relative sizes of the Hill radii (see Fig. 5). The flux is constrained to the assembly rate at the virial radius and to $\phi_{ta} \simeq -32\pi\bar{\rho}H(z)r_{vir}^3 \simeq -9 \times 10^{11} (\frac{r_{vir}}{h^{-1}\text{Mpc}})^3 h^{-1} M_\odot \, \text{Gyr}^{-1}$ at the turnaround radius [assuming that the density at the turnaround radius is $\bar{\rho}$, that $r_{ta} = 2r_{vir}$ and velocity is $- H(z)r_{ta}$]. For the haloes we consider, $r_{vir} \simeq 0.09 \, h^{-1}\text{Mpc}$ and so $\phi_{ta} \simeq -7 \times 10^8 \, h^{-1} M_\odot \, \text{Gyr}^{-1}$. Thus, if all the material that the halo will accrete until $z = 0$ is already within its Hill sphere, then the Hill radius will be on the order of or larger than the turnaround radius. Given that the overdensity within the turnaround radius in the spherical collapse model is found to be 4.56, we can simply compare the overdensity within the estimated Hill radius with this number to compare their relative sizes. We find that the median overdensities within the Hill sphere for the haloes with the 20 per cent highest and lowest assembly rate $A(z)$ at $z = 0.5$ are 5.54 and 12.72, respectively. Thus, for the high-$A(z)$ sample, the relatively low Hill flux is perfectly compatible with their large assembly rates as this is the flux determined close to the turnaround radius. Since their estimated Hill radii are comparable to their turnaround radii, the growth of these haloes is simply unaffected by tides. Indeed, 94 per cent of the high-$A(z)$ and 99 per cent of the low-$A(z)$ sample have at least their final mass contained inside their estimated Hill radius at $z = 0.5$. Note also that in dark-energy cosmologies the value for the turnaround overdensity at low redshifts can be significantly higher than the fiducial Einstein–de Sitter value (see e.g. Horellou & Berge 2005).
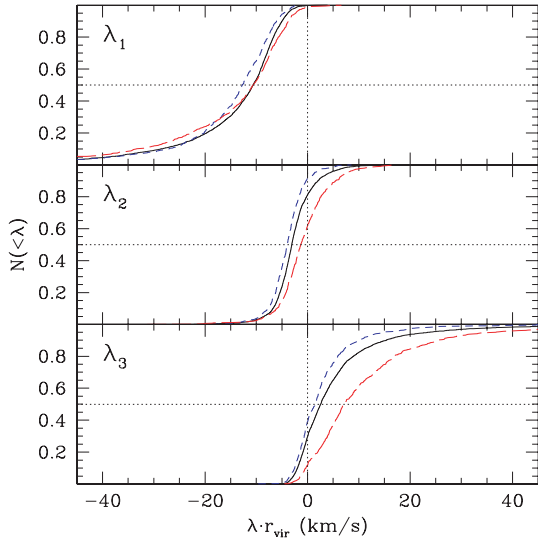
Figure 6. CDFs of the eigenvalues λ_i of the deformation tensor D_{ij}. The data are shown for the $z = 0.5$ progenitors of haloes with masses between 2×10^{10} and $4 \times 10^{10} \, h^{-1} \, \mathrm{M}_\odot$ at $z = 0$. Lines correspond to all these haloes (solid, black), those 20 per cent with highest current assembly rate (short dashes, blue) and those with the lowest (long dashes, red). Stripped haloes are excluded.
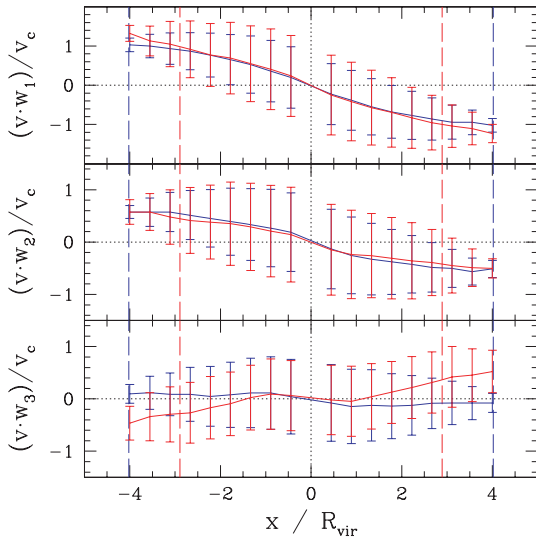

Figure 7. Median velocity field along the three main axes of the rate-of-strain tensor $\boldsymbol{w}_1$ (top), $\boldsymbol{w}_2$ (middle) and $\boldsymbol{w}_3$ (bottom) in units of the halo circular velocity v_c. The data are shown for the $z = 1$ progenitors of haloes with masses between 2×10^{10} and $4 \times 10^{10} \, h^{-1} \, \mathrm{M}_\odot$ at $z = 0$. The sample of haloes is split into those 20 per cent with the largest (blue) and smallest (red) increases in mass. Stripped haloes are excluded. Error bars correspond to the medians (over all haloes) of the 16th and 84th percentiles (computed for each halo). The vertical dashed lines indicate the median Hill radii for the two samples of haloes.

for the presence of an external tidal field. In particular, for the low-A haloes, over 80 per cent have $\lambda_3 > 0$, i.e. the velocity component along the eigenvector associated with λ_3 is positive, particles are moving away from the halo in that direction.

In Fig. 7, we show the median velocity of the environment as a function of distance from the halo centre projected along the three main axes of the rate-of-strain tensor (which coincide with the main

axes of the shear tensor). Results are shown for haloes growing most and least in mass between redshift 1 and 0 for the progenitors of haloes of fixed mass at $z = 0$. The velocity is given in units of the circular velocity of each halo $v_c \equiv \sqrt{\mathrm{GM}/\mathrm{R}_{\mathrm{vir}}}$. While the flow fields are comparable along $\boldsymbol{w}_1$ and $\boldsymbol{w}_2$ apart from slightly larger scatter for the less growing haloes, these haloes show a qualitatively different flow along the eigenvector $\boldsymbol{w}_3$ corresponding to the largest eigenvalue λ_3. For the least growing haloes, along this direction, matter is receding from the halo centre leading to a Hubble-like flow that counteracts infall on to the halo. The data are shown at $z = 1$ where the difference in the flow field is strongest when splitting the halo sample by growth $G(z)$. The scatter shown in Fig. 7 indicates that there is a non-negligible fraction of particles surrounding the halo that have velocities on the order of the halo's circular velocity, as discussed and quantified in the previous section. Note that an outflow along one direction is equivalent to a non-convergent velocity field. Such a non-convergent flow is in excellent agreement with other detections of matter outflows around haloes below the non-linear mass (e.g. Prada et al. 2006).

6 THE ROLE OF TIDAL EFFECTS IN THE ASSEMBLY BIAS

The hierarchical structure formation picture based on the EPS model predicts that the mass of the main progenitor of a halo is determined by the sequence of 'density peaks' on increasingly larger scales that exceed the threshold for collapse. In this picture, formation time depends only on the halo mass without any influence of the environment.

We will argue in this section that in *N*-body simulations, the assembly behaviour of haloes is modulated by tidal effects ranging from the suppression of halo growth to the tidal mass loss due to an encounter with a massive halo in the most extreme cases.

6.1 The influence of tides on halo mass assembly

In order to statistically quantify the interplay between environment and a halo mass assembly, we present Spearman rank correlation coefficients between measures of environment and measures of halo mass assembly in Tables 3 and 4 at three redshifts for the main progenitors of haloes identified at $z = 0$. In Table 3, data are shown for haloes in the $45 \, h^{-1}$ Mpc simulation with masses between 2 and $4 \times 10^{10} \, h^{-1} \, \mathrm{M}_\odot$ at $z = 0$. Table 4 shows the corresponding data for haloes with masses between 2 and $4 \times 10^{11} \, h^{-1} \, \mathrm{M}_\odot$ at $z = 0$ from the $90 \, h^{-1}$ Mpc simulation.

We find that for both mass ranges, the correlation of formation redshift and the eigenvalue λ_3 is strongest at redshifts close to the median formation redshift of the sample. Furthermore, the correlation of assembly rate $A(z)$ with λ_3 increases between redshifts 1 and 0.5 and is significantly stronger for the lower mass sample. Finally, we find that at all redshifts a large λ_3 is strongly correlated with a small growth $G(z)$ and vice versa.

The correlations with λ_3 can now be compared with the dependence of assembly on environment density. At all redshifts above zero, the correlation coefficients between the overdensity in spheres of $2 \, h^{-1}$ Mpc and the three measures of the mass assembly are significantly weaker than those with λ_3. Most remarkably, the correlation between δ_2 and z_{form} is strongest at $z \sim 1$. However, at these times z_{form} correlates significantly stronger with λ_3 than with δ_2, indicating that the density itself is not the primary cause for the suppression. As expected, the correlation between density and λ_3 grows strongly with time.

Table 3. Spearman rank correlation coefficients ρ_s between measures of a halo mass assembly and measures of environment over redshift. Measures of environment are λ_3, the largest eigenvalues of the rate-of-strain tensor, the overdensity δ_S in the shell within one and four virial radii around each halo, δ_2 the matter field smoothed with a spherical top-hat filter of scale $2\,h^{-1}$ Mpc and the deviation from a linear flow $|\boldsymbol{\sigma}|$. Measures of the mass assembly are the formation redshift z_{form}, the assembly rate $A(z)$ and the mass ratio $G(z)$. The coefficients are given for haloes with masses between 2 and $4\times10^{10}\,h^{-1}\,\text{M}_\odot$ at $z=0$. These haloes have a median formation redshift $z_{\text{med}}=1.71$. The median mass $M_{\text{med}}(z)$ of the halo sample at redshift z is given in units of $10^{10}\,h^{-1}\,\text{M}_\odot$. The data are obtained from the $45\,h^{-1}$ Mpc box. Tidally stripped haloes are excluded. These results illustrate that (1) the mass assembly is modulated by λ_3 and (2) the correlation of λ_3 with density grows over time. Bold numbers highlight the correlations with λ_3.

ρ_s	$z=0$	$z=0.5$	$z=1$
$(z_{\text{form}}, \lambda_3(z))$	**0.11**	**0.22**	**0.30**
$(z_{\text{form}}, \delta_2(z))$	0.15	0.17	0.19
$(z_{\text{form}}, |\boldsymbol{\sigma}(z)|)$	0.15	0.18	0.22
$(A(z), \lambda_3(z))$	**−0.13**	**−0.28**	**−0.23**
$(A(z), \delta_2(z))$	−0.18	−0.18	−0.15
$(A(z), |\boldsymbol{\sigma}(z)|)$	−0.17	−0.20	−0.14
$(G(z), \lambda_3(z))$	–	**−0.29**	**−0.32**
$(G(z), \delta_2(z))$	–	−0.13	−0.18
$(G(z), |\boldsymbol{\sigma}(z)|)$	–	−0.19	−0.21
$(\delta_2(z), \lambda_3(z))$	0.60	0.55	0.47
$M_{\text{med}}(z)$	2.7	2.2	1.7

Table 4. Same as Table 3 but for haloes with masses between 2 and $4\times10^{11}\,h^{-1}\,\text{M}_\odot$ at $z=0$. These haloes have a median formation redshift $z_{\text{med}}=1.44$. The data are obtained from the $90\,h^{-1}$ Mpc box.

ρ_s	$z=0$	$z=0.5$	$z=1$
$(z_{\text{form}}, \lambda_3(z))$	**0.09**	**0.22**	**0.27**
$(z_{\text{form}}, \delta_2(z))$	0.15	0.17	0.18
$(z_{\text{form}}, |\boldsymbol{\sigma}(z)|)$	0.11	0.13	0.17
$(A(z), \lambda_3(z))$	**−0.08**	**−0.19**	**−0.08**
$(A(z), \delta_2(z))$	−0.13	−0.14	−0.07
$(A(z), |\boldsymbol{\sigma}(z)|)$	−0.12	−0.13	0.0
$(G(z), \lambda_3(z))$	–	**−0.24**	**−0.31**
$(G(z), \delta_2(z))$	–	−0.12	−0.16
$(G(z), |\boldsymbol{\sigma}(z)|)$	–	−0.11	−0.15
$(\delta_2(z), \lambda_3(z))$	0.65	0.60	0.53
$M_{\text{med}}(z)$	27	21	16

The significance of the quoted correlations can be assessed by testing the hypothesis that $\rho_s(x, z) > \rho_s(y, z)$ for three quantities x, y, z with respect to the fact that x and y are also correlated. This can be calculated using the method of Meng, Rosenthal & Rubin (1992).[5] The Z-scores (significance in units of σ) for the correlations in Tables 3 and 4 are given in Table 5. At redshifts 0.5

[5] The original Meng et al. (1992) test applies for Pearson correlation coefficients but can be easily adopted to rank correlations by replacing all correlation coefficients and multiplying the standard error of the z-transformed values with 1.03 (this is valid for samples larger than 10 and $\rho_s < 0.9$; see Zar 2007).

Table 5. Z-scores $Z(x, y, z)$ reflecting the significance in units of σ that $\rho_s(x, z) > \rho_s(y, z)$ for the correlation coefficients given in Tables 3 and 4. Negative values indicate the score for the alternative hypothesis $\rho_s(x, z) < \rho_s(y, z)$.

	$z=0$	$z=0.5$	$z=1$
$M(0) = 2 - 4 \times 10^{10}\,h^{-1}\,\text{M}_\odot$			
$Z(\lambda_3, \delta_2, z_{\text{form}})$	−2.81	3.71	6.74
$Z(\lambda_3, \delta_2, A)$	2.90	−6.52	−5.03
$Z(\lambda_3, \delta_2, G)$	–	−10.66	−9.24
$M(0) = 2 - 4 \times 10^{11}\,h^{-1}\,\text{M}_\odot$			
$Z(\lambda_3, \delta_2, z_{\text{form}})$	−4.79	3.65	5.76
$Z(\lambda_3, \delta_2, A)$	3.98	−4.08	−0.61
$Z(\lambda_3, \delta_2, G)$	–	−8.78	−10.57

and 1, for all quoted correlation coefficients between A, G and z_{form} with λ_3 and δ_2, the differences are significant at more than 3σ.

We will now briefly discuss the influence of numerical resolution effects in the simulation on these results. Since the mass range of haloes shown in Table 4 is resolved with eight times more particles in the $45\,h^{-1}$ Mpc box, albeit for a smaller sample, we compared all correlation coefficients in the two simulations and found no significant deviations except for the fit residuals $|\boldsymbol{\sigma}|$. At all redshifts, correlations of assembly with $|\boldsymbol{\sigma}|$ were weaker and those with λ_3 slightly stronger in the simulation with a higher mass resolution. The observation that the fit residuals depend on resolution is indicative of a minor resolution dependence in determining the tensor eigenvalues from the flow that results in a slight weakening of correlations with shear. Note also that the quoted results do not change significantly if haloes are selected in a fixed mass range at some redshift $z > 0$ instead of at $z = 0$ except that all correlations with $|\boldsymbol{\sigma}|$ are significantly weaker at redshifts $z > 0$ again reflecting a resolution dependence of the goodness of our CSA model fit to the flow.

6.2 Clustering behaviour of haloes in sheared regions

Tidal fields are strongest in the vicinity of massive haloes where the clustering of smaller haloes is also substantially enhanced. In Fig. 8, we show the correlation functions for haloes with the largest/smallest eigenvalue λ_3 of the rate-of-strain tensor at redshifts zero and their main progenitor haloes at redshift 1. As expected, haloes at redshift 0 with high λ_3 are significantly more clustered than average haloes while those with low λ_3 are less clustered. At redshift 1, the situation is slightly different: only haloes with highest λ_3 are significantly more clustered than average haloes. Furthermore, haloes with the lowest λ_3 show a strong attenuation of the correlation function at distances below $\sim 1\,h^{-1}$ Mpc. This is a clear indication that these haloes are only found in more underdense regions. See also the discussion in Appendix A2 for the dependence of clustering amplitudes on environmental overdensity in the initial density field.

The tidal field, as quantified by the sheared flow around a halo, thus shows a strong correlation with all quantities of the mass assembly as well as the dependence on clustering amplitude that is necessary to account for the halo assembly bias.

6.3 Tidal stripping of halo mass

A halo is prone to tidal mass loss once its Hill radius r_{hill}, defined in equation (10), with respect to a massive neighbour becomes
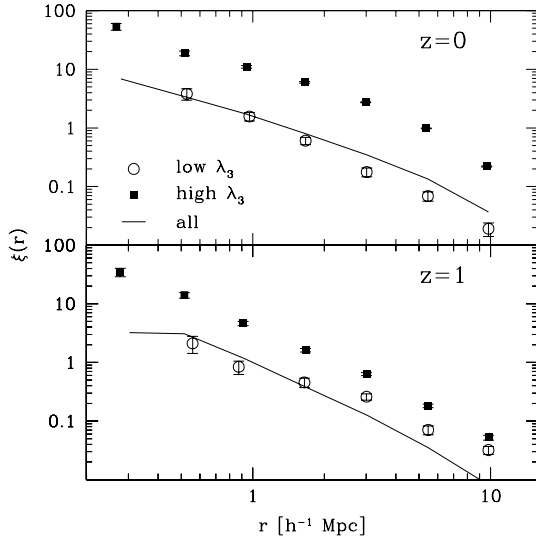
Figure 8. Two-point correlation functions for haloes with masses between 2 and 4×10^{10} at redshift 0. The two panels correspond to these haloes at redshift 0 (top) and their main progenitor haloes at redshift 1 (bottom). The samples have been split into those haloes at the respective redshift with the 20 per cent highest/lowest values in λ_3, the largest eigenvalue of the rate-of-strain tensor. Tidally stripped haloes are not included. Haloes experiencing strong tides, as probed by λ_3, are much stronger clustered than haloes in low shear regions.

smaller than its virial radius $r_{\rm vir}$. Defining haloes as objects with a fixed overdensity $\Delta_{\rm vir}$, we have $m \propto \Delta_{\rm vir} r_{\rm vir}^3$ for the smaller halo and $m \propto \Delta_{\rm vir} r_{\rm vir}^3$ for the larger halo. Then the condition that $r_{\rm hill} < r_{\rm vir}$ is equivalent to

$$d < 3^{1/3} R_{\rm vir} \simeq 1.5 R_{\rm vir}. \tag{19}$$

Thus, a halo is likely to suffer a tidal mass loss once it has approached a more massive halo to within 1.5 virial radii, assuming that the restricted three-body approximation is justified and that the small halo remains nearly spherical. Haloes that tidally lose mass to another halo should be considered as the most extreme case of tidally suppressed mass growth: the range of their gravitational influence has become smaller than their virial radius.

We will now quantify the population of these extreme examples of the tidally truncated mass assembly. As described in Section 4.2, the stripping implies an underestimation of halo mass at $z = 0$ relative to the assembly history at higher z, which is equivalent to an overestimation of the formation redshift. It is thus important for our analysis to quantify the abundance of these objects.

In Fig. 9, we show in grey the fraction of well-resolved haloes in our simulations that are found as isolated haloes at $z = 0$ and lost at least 3 per cent of their particles to a more massive halo (note that this definition entails haloes that are actually detected as subhaloes at $z > 0$.). At a given mass, this fraction is on the order of a few per cent. The fraction is higher for smaller halo masses and reaches a value of $\sim$4.5 per cent for $M \simeq 2 \times 10^{10} \, h^{-1} \, {\rm M}_\odot$.

However, these haloes do not represent the entire population of haloes that underwent a mass loss in an encounter with a more massive halo. First, the time resolution of our saved simulation snapshots does not permit to detect all haloes that were at some point subhaloes of another halo, and second, it is not guaranteed that the tidally unbound mass will be part of the more massive halo after stripping. In order to get an upper limit on their abundance, we consider now all those haloes for which the Hill radius is smaller than the virial radius at some point during their evolution and that
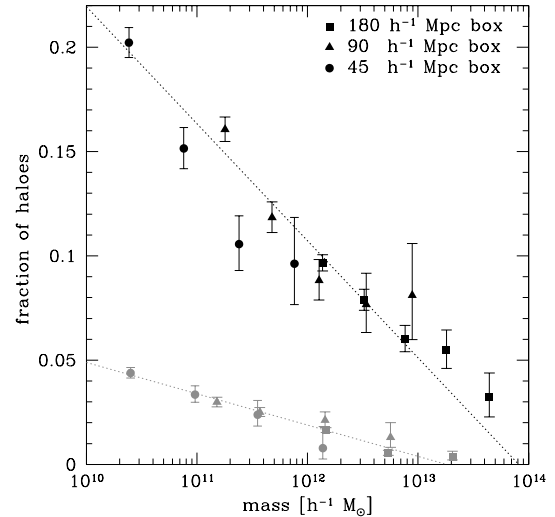

Figure 9. Fraction of haloes that have $r_{\rm Hill} < r_{\rm vir}$ at some point during their evolution (black symbols) and fraction of haloes losing at least 3 per cent of their mass to a more massive halo (grey symbols) as a function of halo mass at redshift $z = 0$. Error bars indicate the 1σ Poisson uncertainties. Results are shown for the three simulations of different resolution described in text. Dotted lines show exponential fits to the data points.

are thus prone to tidal mass loss. The fraction of haloes fulfilling this criterion is on the order of 20 per cent at the lowest masses we considered (see Fig. 9, black line and symbols), in agreement with the results of Diemand et al. (2007) and Dalal et al. (2008). The lower number of those haloes for which actual mass loss is detected implies that the tidally unbound mass typically does not end up in the bigger halo.

In Fig. 1 (left-hand panel), we showed how the correlation of formation redshift with overdensity δ_{2-5} changes when the haloes that lost mass due to an encounter with a more massive object are removed from the sample. The rank correlation decreases from $\rho_s(\delta_{2-5}, z_{\rm form}) = 0.18$ for the entire sample to 0.12 after exclusion of the stripped subset. Removing the larger sample of those haloes that had $r_{\rm Hill} < r_{\rm vir}$ during their evolution also results in a slight increase of the correlation coefficient to 0.16 (all numbers are slightly higher when using δ_2 instead of δ_{2-5}). Note that the criterion $r_{\rm Hill} < r_{\rm vir}$ is roughly equivalent to selecting those haloes that were within 1.5 virial radii of another halo. Our results thus suggest that tidally stripped haloes are only the most extreme cases of a tidally truncated mass assembly.

Furthermore, haloes that are at the apocentre of their orbit after passing through a massive halo are also likely to have very large relative velocities with respect to their environment. Considering the relative velocity between a halo and the surrounding region within 1 and $4 \, r_{\rm vir}$ (cf. Section 5.5), we find that haloes identified as stripped haloes indeed show large relative velocities. These relative velocities will lead to extreme velocity dispersions around haloes and are possibly dominating the results of Wang et al. (2007) (their fig. 8, where median relative velocities are much larger than the halo virial velocity only in the tail of the formation redshift distribution). When removing the stripped haloes, we find that the correlation between relative velocity and formation redshift weakens substantially.

7 DISCUSSION

The formation redshift of dark-matter haloes is highest for haloes that have the lowest assembly rate at late times (cf. Section 4.1).

Tying this suppression of late growth to a physical effect that is most effective in dense/strongly clustered regions can thus potentially explain the correlation of halo clustering and formation redshift, the so-called assembly bias.

Tidal forces induce a sheared flow in the vicinity of small haloes that flow along filaments of the cosmic web (Section 5.1). To quantify this effect, we measured the local influence of the larger-scale tidal field by considering the rate-of-strain tensor of the flow in the immediate vicinity of haloes. We found that the progenitors of haloes of a given mass at $z = 0$ that have the lowest mass assembly rates experience significantly stronger shear during their assembly history than those haloes with high mass assembly rates.

Tidal effects are expected to be strongest in the vicinity of massive haloes. Whenever a mass M at a distance r from a smaller halo completely dominates the potential, the tide in the direction of this mass is given by $2GM/r^3$, while the perpendicular tides are given by $-GM/r^3$. In the rest frame of the smaller halo, matter is receding along the direction to the massive halo. Furthermore, upon approaching the massive halo, the environment density will grow substantially and as a consequence the correlation between density and shear grows with time (see Section 6). Since the abundance of small haloes is enhanced near massive haloes, the population of tidally suppressed haloes will be biased such that a dependence of formation redshift on clustering amplitude and environment density arises as a secondary effect. The more fundamental character of tides is reflected in the stronger correlation of measures of halo growth with λ_3 than with environment density (Section 6).

The tidal influence of a larger halo on the accretion properties of neighbouring smaller haloes can be readily understood from the restricted three-body problem. Stable orbits around the smaller halo exist only within its Hill sphere (see Section 5.3). A halo can only accrete particles (and other smaller haloes) in the presence of a massive halo if they are contained in the Hill sphere. The radius of the Hill sphere shrinks linearly with the distance to the massive neighbour so that the amount of matter available for accretion becomes increasingly smaller. In addition, a halo is prone to mass loss when the Hill radius becomes smaller than its virial radius. As shown in Section 6.3, this happens roughly at a distance of 1.5 virial radii of the larger halo.

In the most extreme cases, small haloes can undergo a very strong tidal mass loss when passing through the massive halo. A minor fraction of haloes of a given mass are indeed not typical isolated haloes since they are once again found outside the virial radius of a massive halo after their first pericentre passage through its potential well. These haloes have also been observed in resimulations of single massive haloes (Gill et al. 2005; Diemand et al. 2007; Ludlow et al. 2008).

While a tidal mass loss inside the virial radius of another halo is the most violent and non-linear example, tidal suppression of halo growth seems to be already present in the quasi-linear regime. Keselman & Nusser (2007) recover the assembly bias also using the punctuated Zel'dovich approximation where the mass of haloes grows monotonously by definition, and a tidal mass loss is thus impossible.

We explore the link between assembly bias and the initial linear density field in Appendix A where we compare the masses of haloes measured from the simulations with the masses they should reach in an isolated environment according to the EPS model. Our results indicate that the EPS-predicted masses are roughly a factor of 2–3 higher for the oldest haloes than for the youngest. Furthermore, we find a significant correlation between this mismatch and both the strength of the shear and large-scale density at $z = 0$ in the simulation. This provides further evidence that indeed the environment, that is not considered when determining the EPS-like masses, prevents the mass from growing to the predicted value. Hence, while the EPS would predict that the halo will assemble mass, the strong shear that the EPS does not account for prevents this (see also van de Weygaert & Babul 1994). If the correct final mass is known, it can be shown that the density dependence of formation redshifts can be reproduced using a simple peak-background-split model (see Appendix A).

A question that is opened by our analysis is whether the last major merger of small haloes occurs preferentially perpendicular to their host filament such that the mechanism we described is potentially also related to alignments between halo spins and shapes and the surrounding large-scale structure (e.g. Dekel 1985). For small galactic dark-matter haloes, such strong alignments between halo shape and the direction to the nearby cluster have been found by Pereira, Bryan & Gill (2008) extending out to many virial radii of the cluster and by alignments of both halo shape and spin with host filaments and sheets by Hahn et al. (2007a) and Aragón-Calvo et al. (2007) (see also Basilakos et al. 2006; Ragone-Figueroa & Plionis 2007). Lee & Erdogdu (2007) claim observational evidence for an alignment of galaxy spins with the reconstructed tidal field. In the picture outlined in this paper, the decreased probability for mergers or accretion along the filament would preserve the spin vector alignment with the filament/sheet which is established when merging occurs preferentially perpendicular to the filament/sheet.

We focused in this paper on the role of tidal effects in the assembly of haloes in different environments. We note that other global properties of haloes, such as the substructure in them and their spin parameter, also correlate with environment (see e.g. Wechsler et al. 2006; Gao & White 2007; Bett et al. 2007). The possible relation between these properties and the suppression of accretion on to haloes should be explored.

8 SUMMARY AND CONCLUSIONS

Using a series of cosmological N-body simulations, we demonstrated that the mass assembly of haloes is influenced by tidal effects in the vicinity of massive haloes. The resulting suppression of mass growth at late times is reflected in an increase in formation redshift. The space density of small haloes near massive haloes is enhanced (since their spatial cross-correlation is high and positive). Thus, as a secondary effect, a tidally suppressed assembly of halo masses directly translates into biased spatial distributions of young and old haloes identified at $z = 0$: old haloes will be found more likely in regions of high density than younger haloes.

The presence of tides has an important effect on the infall behaviour on to a halo. To quantify this, we measured the influence of external tides by considering the rate-of-strain tensor, and especially its largest eigenvalue λ_3, fitted to the flow between 1 and 4 virial radii around haloes. In detail, we found the following for small haloes.

(i) High formation redshift is related to a low assembly rate at late times. Thus, any spatially biased process that suppresses mass growth at late times can potentially lead to an age-dependent bias of halo clustering.

(ii) Among all measures of environment that we considered, assembly rate at redshifts $z > 0$ correlates most strongly with the largest eigenvalue λ_3 of the rate-of-strain tensor, and especially so when measured at high redshift, $z \sim 1$. The correlation of assembly rate with the density of the environment is weaker. We find that

haloes with a low assembly rate have suppressed infall or even out-
flow in the region between 1 and 4 virial radii along one direction.
Furthermore, we find that this direction corresponds, with little scat-
ter, to the direction to that neighbouring halo that has the strongest
tidal influence.

(iii) The strain eigenvalue λ_3 (probing velocity shear) is strongly
correlated with the tidal field due to the neighbouring halo that
exerts the strongest tides. This correlation has been verified using
a restricted three-body approximation for the tidal field. Thus, tidal
forces induce a velocity shear in the flow around dark-matter haloes
and can render accretion ineffective by altering the convergence of
the accretion flow on to a halo.

(iv) The correlation between λ_3 (probing velocity shear and tides)
and density grows with time. Thus, haloes in strongly sheared re-
gions are much more strongly clustered than average and associated
with high-density regions on to which they fall. Hence the suppres-
sion of mass growth is stronger in regions of high density.

(v) Haloes can undergo a mass loss due to the tidal influence of
a larger halo when their Hill radii become smaller than their virial
radii. This already happens at a distance of 1.5 virial radii of the
larger halo and will be most severe inside its virial radius. Roughly
20 per cent of the 2–$4 \times 10^{10}\, h^{-1}\, \mathrm{M}_\odot$ fulfil the condition for mass
loss at some point of their history. These haloes are the most extreme
cases of tidal suppression of assembly.

(vi) The mismatch between the mass that the EPS formalism can
be attributed to a halo, and the mass that is measured for it in the
simulation correlates with formation time and with the eigenvalue
λ_3 indicating a dependence of this mismatch on tides (this is shown
in the appendix).

From the evidence presented above, we conclude that the tidal
field due to neighbouring massive haloes exerts a shear on the flow
surrounding small haloes. In the rest frame of the small halo, this
is an outward flow along the direction to the more massive halo,
tidally suppressing the growth of the small halo. This is especially
effective in filaments since most of the matter is located along the
direction from which it is least effective for the halo to accrete.

The proximity to more massive haloes, where the clustering is
enhanced, leads to a spatial bias of haloes that experience strong
tides, especially haloes below the non-linear mass, and thus also to
a bias of the population of 'old' and 'young' haloes of the same
mass. We conclude that this is an important factor in the emergence
of the *assembly bias*.

ACKNOWLEDGMENTS

REFERENCES

Angulo R. E., Baugh C. M., Lacey C. G., 2008, MNRAS, 387, 921
Aragón-Calvo M. A., van de Weygaert R., Jones B. J. T., van der Hulst J. M., 2007, ApJ, 655, L5
Bardeen J. M., Bond J. R., Kaiser N., Szalay A. S., 1986, ApJ, 304, 15
Barnes A., Rowlinson R. R., 1989, Class. Quantum Gravity, 6, 949
Basilakos S., Plionis M., Yepes G., Gottlöber S., Turchaninov V., 2006, MNRAS, 365, 539
Bertschinger E., 2001, ApJS, 137, 1
Bertschinger E., Jain B., 1994, ApJ, 431, 486
Bett P., Eke V., Frenk C. S., Jenkins A., Helly J., Navarro J., 2007, MNRAS, 376, 215
Bond J. R., Cole S., Efstathiou G., Kaiser N., 1991, ApJ, 379, 440
Catelan P., Lucchin F., Matarrese S., Porciani C., 1998, MNRAS, 297, 692
Cleveland W. S., 1979, J. Am. Stat. Assoc., 74, 829
Cooray A., Sheth R., 2002, Phys. Rep., 372, 1
Croton D. J., Gao L., White S. D. M., 2007, MNRAS, 374, 1303
Dalal N., White M., Bond J. R., Shirokov A., 2008, ApJ, 687, 12
Davis M., Efstathiou G., Frenk C. S., White S. D. M., 1985, ApJ, 292, 371
Dekel A., 1985, ApJ, 298, 461
Desjacques V., 2008, MNRAS, 388, 638
Diemand J., Kuhlen M., Madau P., 2007, ApJ, 667, 859
Doroshkevich A. G., 1970, Astrophysics, 6, 320
Efstathiou G., Frenk C. S., White S. D. M., Davis M., 1988, MNRAS, 235, 715
Fakhuri O., Ma C.-P., 2009a, MNRAS, 394, 1825
Fakhuri O., Ma C.-P., 2009b, preprint (arXiv:0906.1196)
Gao L., White S. D. M., 2007, MNRAS, 377, L5
Gao L., Springel V., White S. D. M., 2005, MNRAS, 363, L66
Gill S. P. D., Knebe A., Gibson B. K., 2005, MNRAS, 356, 1327
Hahn O., Carollo C. M., Porciani C., Dekel A., 2007a, MNRAS, 381, 41
Hahn O., Porciani C., Carollo C. M., Dekel A., 2007b, MNRAS, 375, 489
Harker G., Cole S., Helly J., Frenk C., Jenkins A., 2006, MNRAS, 367, 1039
Horellou C., Berge J., 2005, MNRAS, 360, 1393
Jing Y. P., Suto Y., Mo H. J., 2007, ApJ, 657, 664
Keselman J. A., Nusser A., 2007, MNRAS, 382, 1853
Klypin A., Hoffman Y., Kravtsov A. V., Gottlöber S., 2003, ApJ, 596, 19
Lacey C., Cole S., 1993, MNRAS, 262, 627
Lee J., Erdogdu P., 2007, ApJ, 671, 1248
Li Y., Mo H. J., Gao L., 2008, MNRAS, 389, 1419
Ludlow A. D., Navarro J. F., Springel V., Jenkins A., Frenk C. S., Helmi A., 2009, ApJ, 692, 931
Maulbetsch C., Avila-Reese V., Colín P., Gottlöber S., Khalatyan A., Steinmetz M., 2007, ApJ, 654, 53
Meng X., Rosenthal R., Rubin D. B., 1992, Psychological Bull., 111, 172
Mo H. J., White S. D. M., 1996, MNRAS, 282, 347
Mo H. J., Yang X., van den Bosch F. C., Katz N., 2005, MNRAS, 363, 1155
Murray C. D., Dermott S. F., 2000, Solar System Dynamics. Cambridge Univ. Press, Cambridge
Neistein E., Dekel A., 2008, MNRAS, 383, 615
Neistein E., van den Bosch F. C., Dekel A., 2006, MNRAS, 372, 933
Pereira M. J., Bryan G. L., Gill S. P. D., 2008, ApJ, 672, 825
Porciani C., Dekel A., Hoffman Y., 2002a, MNRAS, 332, 325
Porciani C., Dekel A., Hoffman Y., 2002b, MNRAS, 332, 339
Prada F., Klypin A. A., Simonneau E., Betancort-Rijo J., Patiri S., Gottlöber S., Sanchez-Conde M. A., 2006, ApJ, 645, 1001
Press W. H., Schechter P., 1974, ApJ, 187, 425
Ragone-Figueroa C., Plionis M., 2007, MNRAS, 377, 1785
Sandvik H. B., Möller O., Lee J., White S. D. M., 2007, MNRAS, 377, 284
Sheth R. K., Tormen G., 2004, MNRAS, 350, 1385
Springel V., 2005, MNRAS, 364, 1105
Taruya A., Suto Y., 2000, ApJ, 542, 559
van de Weygaert R., Babul A., 1994, ApJ, 425, L59
van den Bosch F. C., 2002, MNRAS, 331, 98
Wang H. Y., Mo H. J., Jing Y. P., 2007, MNRAS, 375, 633
Wechsler R. H., Bullock J. S., Primack J. R., Kravtsov A. V., Dekel A., 2002, ApJ, 568, 52
Wechsler R. H., Zentner A. R., Bullock J. S., Kravtsov A. V., Allgood B., 2006, ApJ, 652, 71
Wetzel A. R., Cohn J. D., White M., Holz D. E., Warren M. S., 2007, ApJ, 656, 139
Zar J. H., 2007, Biostatistical Analysis. Prentice-Hall, USA
Zel'dovich Y. B., 1970, A&A, 5, 84

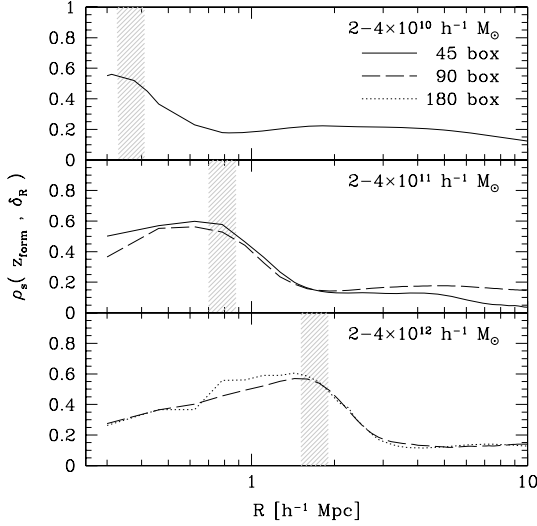**Figure A1.** Spearman rank correlation coefficient ρ_s between halo formation redshift z_{form} and 'peak height' of the Lagrangian density field smoothed with a real space top-hat filter on scale R as a function of the filter scale. Results are shown for three mass ranges. Results for the different simulations are indicated by different line styles. The shaded regions indicate the half-mass range $M/2$ for the corresponding mass bins. This analysis reveals (1) the correlation coefficient peaks as expected for haloes of mass M on scales around $M/2$ and (2) the correlation with the large-scale density field on several h^{-1} Mpc is significant.

APPENDIX A: ASSEMBLY BIAS IN THE INITIAL DENSITY FIELD

A1 Predicting the assembly bias from the initial density field

Can we predict the amplitude of the assembly bias directly from the linear density field? This requires being able to forecast the formation redshift, final mass and local Eulerian density of a halo directly from the initial conditions.

A1.1 Halo formation redshift

What determines the formation redshift of a halo? In Fig. A1, we show the Spearman rank correlation coefficient between the formation redshift z_{form} and the linear overdensity field evaluated at the centre of mass of the Lagrangian patch that will form a halo at $z = 0$. The overdensity field is computed after smoothing the density field with a top-hat filter of radius R. The rank correlation coefficients with z_{form} are plotted against R. Our results show that the formation time of a halo of mass M is most strongly determined by the value of the linear overdensity smoothed on a scale $\sim M/2$. This is what one trivially expects for spherical perturbations. Tides on slightly larger scales (but still internal to the protohalo) also correlate with z_{form}, but to a lesser degree (not shown in the figure). The tidal suppression of halo assembly discussed in the previous sections manifests itself in the initial conditions as a residual correlation between z_{form} and δ_R for large smoothing scales. The rank correlation coefficient is as high as 0.2 even for smoothing radii of a few Mpc. The presence of nearby density fluctuations influences the formation time of a given halo.

A1.2 The assembly bias

If the final halo masses are known, the assembly bias can be perfectly reproduced starting from the initial density field and using
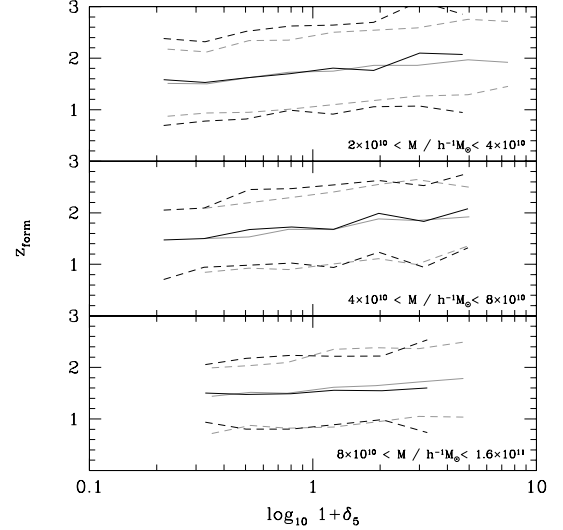

Figure A2. Halo formation time as a function of environmental density on scales $5\,h^{-1}$ Mpc obtained from the N-body simulations (grey) and obtained from the initial conditions data using a combination of two spherical collapse models for the evolution of the background and the peak (black), the mass of the halo is taken from the N-body simulation. Stripped haloes are not considered. Solid lines indicate the median and dashed lines indicate the $\pm 1\sigma$ spread around the median.

a simple peak-background-split model where small-scale fluctuations are responsible for halo collapse, and large-scale fluctuations determine the local density of the halo environment.

Inspired by Fig. A1, we assume that the formation redshift $\hat{z}_{form}$ of a halo of mass M is fully determined by the 'peak height' $\delta_{M/2}$. Denoting by $D_+(z)$ the linear growth factor of density fluctuations, we thus solve the condition for collapse of a spherical density perturbation

$$\frac{D_+(\hat{z}_{form})}{D_+(z_i)}\,\delta_{M/2} = \delta_c, \qquad (A1)$$

where z_i is the initial redshift. We find that a value of $\delta_c = 2.3$ leads to the best agreement between $\hat{z}_{form}$ and z_{form} obtained from the N-body simulation.

In a second step, we determine the evolution of the background density field δ_5 on scales of $R_b = 5\,h^{-1}$ Mpc. Small haloes that survive until $z = 0$ will preferentially form in regions that are underdense on these scales in the initial density field. They will then migrate into regions of higher density over time. We determine the evolution of the background density using first-order Lagrangian perturbation theory. Given the eigenvalues Λ_i of the initial tidal field on scales of $R_{b,0}$, the evolution of δ_5 at the positions of the haloes is given before shell crossing by

$$\delta_5(z) = \frac{1}{\prod_{i=1}^{3}\left[1 - D_+(z)\,\Lambda_i\right]} - 1 \qquad (A2)$$

in the Zel'dovich approximation (Zel'dovich 1970).

For each halo in the N-body simulation, we thus obtain an environmental density at $z = 0$ and the redshift of collapse $\hat{z}_{form}$ by knowing a priori its final mass and its Lagrangian position. In Fig. A2, we show the median formation redshift $\hat{z}_{form}$ (in grey) as a function of density δ_5 for three mass bins.[6] The corresponding relation is shown also for the quantities directly obtained from the

---

[6] We have checked that results are not influenced by the small fraction of haloes that already experienced shell crossing on the $5\,h^{-1}$ Mpc scale.
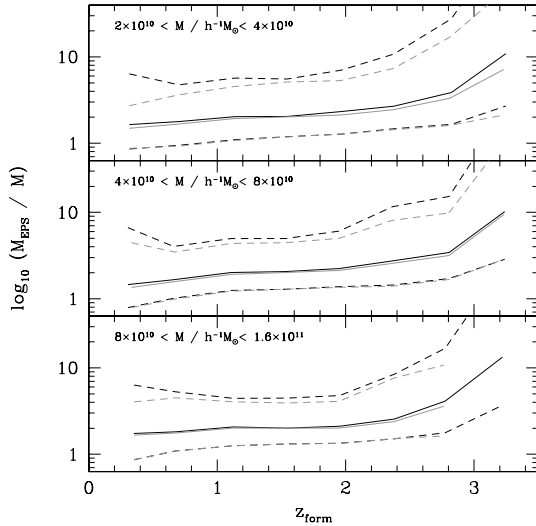
Figure A3. The ratio of the mass determined in the initial conditions using the EPS model to the mass measured in the *N*-body simulation as a function of halo formation time. Solid lines indicate the median and dashed lines indicate the 16th and 84th percentiles. Shown is the relation for haloes that are not undergoing tidal mass loss (grey) and for all haloes (black) in three mass bins.

N-body simulation (in black). We find very good agreement with the *N*-body data suggesting that this simple model suffices to predict the correlation between formation redshift and environment seen in the simulations if the correct final mass is known.

Replacing the actual halo masses with those predicted at the Lagrangian halo locations by the EPS formalism is sufficient to completely erase any dependence of the formation redshift on environmental density. The spherical collapse model (on which the EPS method is based) tends to overestimate halo masses, particularly for those haloes that are located within strongly sheared flows. In Fig. A3, we show how the formation redshift z_{form} depends on the ratio between the mass M_{EPS} and the mass M, where z_{form} and M are determined from the *N*-body simulations. We find that the mismatch increases from a median ratio of about 1.5 at low formation redshifts to about 3 at high formation redshifts for the considered masses (cf. fig. 3 in Wang et al. 2007). When we exclude the mass-stripped haloes (grey lines), the scatter is significantly reduced. The ratio between the EPS-predicted mass and the mass found in the *N*-body simulations correlates with the largest eigenvalue λ_3 of the rate-of-strain tensor as strongly as with the halo formation redshift. For haloes at $z = 0$ with masses between 2 and 4 $\times$ $10^{10} \, h^{-1} \, M_\odot$, the Spearman rank correlation coefficient between M_{EPS}/M and the shear eigenvalue λ_3 is 0.29. It is 0.27 between M_{EPS}/M and z_{form}. This provides further evidence that tidally suppressed accretion is responsible for the existence of the assembly bias. The proximity to a massive halo is reflected in the correlation coefficient with density obtained with the top-hat filter at $z = 0$. We find that the correlation coefficient with M_{EPS}/M is 0.22 for density determined on scales of $5 \, h^{-1}$ Mpc, 0.31 for $2 \, h^{-1}$ Mpc and 0.41 for $0.5 \, h^{-1}$ Mpc.

A2 Lagrangian assembly bias

It is interesting to verify whether the assembly bias is already present in the spatial distribution of protohaloes in the linear density field.
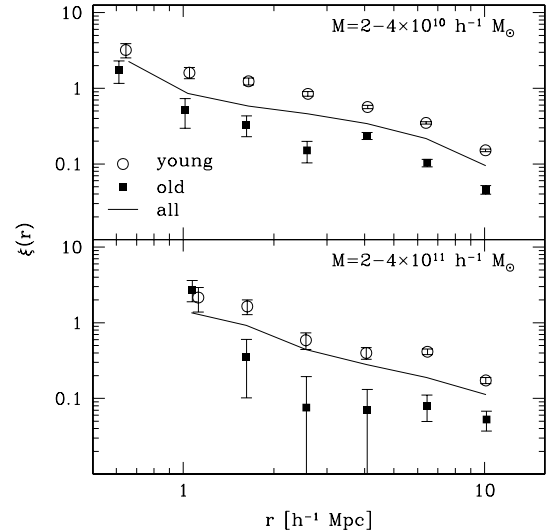

Figure A4. Two-point correlation functions of the Lagrangian centres of mass in the initial density field ($z = 78.5$) for haloes with masses 2–4 $\times$ $10^{10} \, h^{-1} \, M_\odot$ at $z = 0$ (upper panel) and 2–4 $\times 10^{11} \, h^{-1} \, M_\odot$ (lower panel). The solid line shows the correlation function for all haloes, while open circles and filled squares correspond to the 10 per cent of these haloes with the lowest and highest formation redshifts, respectively.

The Lagrangian bias is given by $b_L = b_E - 1$ if b_E is the Eulerian bias (e.g. Mo & White 1996). For $M < M_*$ haloes, $b_E < 1$. Thus, if $b_{E,old} > b_{E,young}$ it follows that $0 \geq b_{L,old} > b_{E,young}$ and thus the old haloes should have a lower Lagrangian clustering amplitude than the young ones.

To verify this, we compute the two-point correlation of the Lagrangian patches of old and young haloes (selected at $z = 0$) at the initial redshift of our simulations. Fig. A4 shows the correlation function of the protohaloes that will form objects with masses between 2 and $4 \times 10^{10} \, h^{-1} \, M_\odot$ at $z = 0$. The corresponding correlations at $z = 0$ have been presented in Fig. 1. At $z = 0$, the oldest haloes cluster more strongly than the youngest ones. For the Lagrangian patches, as expected, the opposite is true: the oldest (youngest) haloes are significantly less (more) clustered than the total. This indicates that, already in the linear density field, the environments surrounding the Lagrangian patches of young and old haloes have different properties. In particular, we find that both young and old haloes at these masses form in initially underdense (i.e. with a median $\delta_5 < 0$) regions. However, the Lagrangian patches of young protohaloes reside (on average) in more underdense regions which, in a Gaussian random field, are more strongly clustered. Using the mean squared overdensities at the halo centres as a proxy for their clustering amplitude (i.e. assuming a linear bias model independent of halo age for the halo density), $B = \langle \delta_5^2 \rangle^{1/2}$, we find $B_{old}/B_{all} = 0.8$ and $B_{young}/B_{all} = 1.2$. On the other hand, with time, the protohaloes will collapse and flow towards denser regions thus changing their clustering properties. At $z = 0$, we find $B_{old}/B_{all} = 1.8$ and $B_{young}/B_{all} = 0.33$. The reversal of the assembly bias is then a simple result of the evolution of the halo environmental density. Older haloes have thus always resided in more overdense regions than younger haloes.